Article, Author's Postprint

**Kunz, Michael; Wassermann, Stefanie**

# Characteristics and sensitivity of orographic precipitation to changing ambient conditions

Meteorologische Zeitschrift



**Erstveröffentlichung in Meteorologische Zeitschrift 2 (2011), S. 199-215.**
Für eine korrekte Zitierbarkeit ist die Seitennummerierung
der Originalveröffentlichung für jede Seite kenntlich gemacht. 

# Sensitivity of flow dynamics and orographic precipitation to changing ambient conditions in idealised model simulations

Michael Kunz[a*] und Stefanie Wassermann[a,b]

[a] Institute for Meteorology and Climate Research, Karlsruhe Institute of Technology (KIT), Germany
[b] Now at: Federal Waterways Engineering and Research Institute (BAW), Karlsruhe, Germany

*Corresponding author: Michael Kunz, Institute for Meteorology and Climate Research, Karlsruhe Institute of Technology (KIT), Kaiserstraße 12, 76128 Karlsruhe, Germany, e-mail: kunz@kit.edu

Idealised numerical simulations using the non-hydrostatic weather prediction model of the Consortium for Small-scale Modeling (COSMO) in a three-dimensional (3D) configuration were conducted to investigate the relationship between ambient conditions, flow characteristics, and orographic precipitation patterns. By changing the model input parameters of wind speed, static stability, temperature, and relative humidity, different flow effects from conditionally unstable flow to upstream deceleration are considered. It is shown that latent heat release significantly delays the onset of flow stagnation, which can be understood using the moist stability concept. However, due to the vertical variations of saturated and unsaturated layers, it is not possible to apply this concept for determining gravity waves. Both the drying ratio, expressing the conversion of the upstream moisture flux into precipitation, and the location of the precipitation maxima can be described to a certain extent by the saturated nondimensional mountain height, $M_m = N_m H/U$, where $H$ is the mountain height, $N_m$ is the saturated stability, and $U$ is the undisturbed wind speed. In the flow around regime, the precipitation maxima are associated with the extended gravity wave and are located downstream of the mountain crest. With increasing direct mountain overflow (decreasing $M_m$), the precipitation maxima are shifted to a location upstream of the crest. The transition from purely stratiform precipitation to embedded convection occurs abruptly when $M_m$ becomes imaginary, indicating conditional instability.

## Zusammenfassung

Idealisierte numerische Simulationen mit dem nicht-hydrostatischen Wettervorhersagemodell des Konsortiums für kleinskalige Modellierung (COSMO) in einer dreidimensionalen (3D) Konfiguration wurden durchgeführt, um den Zusammenhang zwischen Umgebungsbedingungen, Strömungscharakteristika und räumlichen Mustern des orografisch bedingten Niederschlags zu untersuchen. Durch Änderung der Eingabeparameter des Modells wie Windgeschwindigkeit, Stabilität, Temperatur und relative Feuchte werden verschiedene Strömungsbereiche von bedingt instabiler bis zu stagnierender Strömung berücksichtigt. Es wird gezeigt, dass latenter Wärmeübergänge den Be-

ginn der Stagnation der Strömung erheblich verzögern, was mittels des Konzepts der gesättigten Stabilität nachvollzogen werden kann. Aufgrund der vertikalen Variation der Sättigungsbereiche kann dieses Konzept jedoch nicht für die quantitative Beschreibung von Schwerewellen herangezogen werden. Sowohl das Trocknungsverhältnis, das die Umwandlung des Wasserdampfflusses stromauf in Niederschlag angibt, als auch die Position der Niederschlagsmaxima lassen sich bis zu einem gewissen Grad durch die gesättigte dimensionslose Berghöhe $M_m = N_m H/U$ beschreiben mit $H$ als Berghöhe, $N_m$ als gesättigte Stabilität und $U$ als ungestörte Anströmgeschwindigkeit. Bei der Umströmung des Bergs werden die Niederschlagsmaxima durch die ausgedehnte Schwerewelle stromab bestimmt. Mit zunehmender direkter Überströmung (Abnahme $M_m$), verlagern sich die Maxima stromauf des Gipfels. Der Übergang von rein stratiformen Niederschlägen zu eingelagerter Konvektion vollzieht sich abrupt wenn $M_m$ imaginär wird und eine bedingt labile Schichtung vorliegt.

## 1 Introduction

Mountain barriers and related dynamics such as upslope ascent, downslope descent, or the formation of gravity waves strongly modify the amount and spatial distribution of precipitation. If orographically induced ascent dominates synoptic-scale lifting, precipitation upstream of the mountain can be significantly enhanced, which may trigger floods, landslides, or avalanches. Accurate assessment of orographic precipitation therefore is a prerequisite for water and risk management

When impinging on a mountain, the air flow may be perturbed significantly depending on the horizontal and vertical dimensions of the obstacle, thermal stratification, wind speed, and moisture load. In the past, the different flow phenomena evolving over the mountains were studied by many authors under non-saturated conditions and related to the mountain Froude number $Fr = U(NH)^{-1}$ (or nondimensional mountain height $M = Fr^{-1}$), where $U$ and $N$ are the background wind speed and thermal stratification in terms of Brunt-Väisälä frequency, respectively, and $H$ is the mountain height (e.g., PIERREHUMBERT and WYMAN, 1985; DURRAN, 1990). From analytic solutions for special setups (LYRA, 1943; QUENEY, 1948; WURTELE, 1957)

Kunz, Wassermann: Sensitivity of flow dynamics and orographic precipitation to changing ambient conditions in idealised model simulations
Meteorologische Zeitschrift 2 (2011), S. 199-215.
S. 200

and numerical model studies (SMOLARKIEWICZ and ROTUNNO, 1989; DURRAN, 1990; SCH¨A R and DURRAN, 1997), it is known that small Froude number flow ($Fr < 1$) is associated with nonlinear effects like upstream blocking and flow around the mountain and/or wave breaking aloft (e.g., SMOLARKIEWICZ and ROTUNNO, 1989; BAINES and SMITH, 1993; SMITH and GRØNÅS,

1993). At a high Froude number ($Fr > 1$), the flow tends to pass directly over the mountain and vertically propagating or trapped lee waves may form (MILES and HUPPERT, 1969; SMITH, 1989), which can be described properly by linear theory according to SMITH (1979).

The various flow phenomena occurring over mountains are also decisive for the intensification or decrease of precipitation. In case of saturation, however, the flow may be modified also by diabatic effects due to phase transitions, i.e. condensation during ascent or evaporation during descent. As shown by DURRAN and KLEMP (1983), inclusion of moisture reduces static stability, which in turn weakens the amplitude of the gravity waves. In several modelling studies, this effect is considered by applying the moist stability concept, where the dry Brunt-Väisälä frequency $N_d$ is substituted by the saturated equivalent $N_m$ in the diagnostic relations. JIANG (2003), for example, demonstrated that latent heat release and precipitation can significantly delay the onset of mountain flow stagnation. He showed that windward flow stagnation over an idealised Gaussianshaped hill may still be predictable, if the corresponding $N_m$ can be properly estimated from the background flow. Besides, he found that the effect of flow blocking and splitting on the intensity and distribution of orographic precipitation may be significant. Based on idealised sensitivity studies, COLLE (2004) examined the effect of mountain height and width, wind speed, moist static stability, and freezing level on orographic precipitation using a 2D version of 5th generation mesoscale model (MM5). He showed that the precipitation distribution is very sensitive to the structure of terraininduced gravity waves and the occurrence of flow blocking. According to the idealised model study of ZÄNGL (2008), the location of the precipitation maxima is also controlled by the level of the melting layer. If this level is approximately at the height of the mountain peaks, precipitation occurs both upstream and downstream of the mountain top, whereas lower or higher freezing levels cause downstream precipitation only.

These modelling studies were complemented by several observational analyses to gain a better and comprehensive understanding of orographically-modified flow and the repercussion to orographic precipitation. Within the frame of the Mesoscale Alpine Programme (MAP) in 1999, STEINER et al. (2003) found that diabatic effects, indicated by changes in the Froude number, may strongly modify the amount and spatial distribution of orographic precipitation within large Alpine valleys. For an intensive observation period (IOP8) with high loads of stratiform precipitation, they showed that the underestimation of flow blocking in numerical models was the main source of error in quantitative precipitation forecasts. According to MEDINA and HOUZE (2003), stable thermal stratification close to the ground due to diabatic cooling by phase transitions and in combination with low wind speeds ($Fr < 1$) prevented air layers below 900 hPa from being lifted over the mountains. For $Fr > 1$ also air masses close to the ground were lifted directly over the mountains and a pronounced lifting and precipitation area form upstream of the crest. During MAP IOP2a, substantial orographic enhancement of precipitation was observed when air masses close to the ground were lifted over the obstacles at $Fr >> 1$ (HOUZE et al., 2001; MEDINA and HOUZE, 2003). Further studies report a direct relationship between orographic precipitation and the Froude number. CARBONE et al. (1998), for example, found a relation between both parameters over the mountains of Hawaii, while SINCLAIR et al. (1997) stated that the Froude number can explain most of the variations of the spillover across the Southern Alps of New Zealand. Over the low mountain ranges of the Black Forest,

KUNZ and KOTTMEIER (2006a) established a relation between precipitation and dry Froude number.

The goal of this paper is to investigate the dynamical and microphysical effects that evolve in saturated flows and how they affect the amount and spatial distribution of orographic precipitation. The investigations are based on different sets of three-dimensional (3D) simulations for idealised conditions using a numerical weather prediction model. To ease the interpretation of the precipitation patterns, the simulations are greatly simplified and use a few basic parameters such as wind speed, static stability, temperature, and relative humidity only. Sensitivity of orographic precipitation is examined by successively changing these parameters according to realistic mid-latitude settings. Because heavy precipitation due to stable ascent over low-mountain ranges often results in flooding in Central Europe (e.g., ULBRICH et al., 2003; KUNZ and KOTTMEIER, 2006b), advancing the knowledge of orographic precipitation within this parameter space may also help to better understand the problems and limits often inherent in quantitative precipitation forecasts. In addition, a better understanding of how small changes in the ambient conditions modify orographic precipitation forecasts is an important issue in the perspective of ensemble forecasts.

The main scientific questions that will be addressed in this study are: (i) how does inclusion of moisture affect flow conditions in terms of flow deceleration upstream of the hill and vertical wavelength, (ii) how do mountain gravity waves and related microphysics affect the distribution of orographic precipitation, (iii) how do orographic precipitation patterns change as the static stability and flow strength vary, and (iv) is it possible to

Kunz, Wassermann: Sensitivity of flow dynamics and orographic precipitation to changing ambient conditions in idealised model simulations
Meteorologische Zeitschrift 2 (2011), S. 199-215.
S. 201

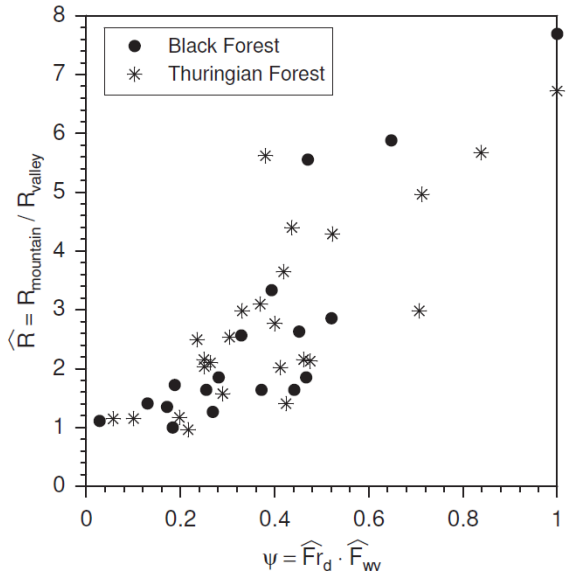


Figure 1: Ratio of 24-hour rainfall totals $\hat{R}$ between a mountain and an adjacent valley station as a function of the precipitation sensitivity $\psi$, which is the product of dry Froude number $Fr_d$ and horizontal incoming water vapour flux $F'_{wv}$ (normalised by their maximum values). Results are shown for the low mountain ranges of Black Forest (stations: Emmendingen, 203 m MSL / Schönwald, 1025 m) and southern Thuringian Forest (Coburg, 322 m / Neuhaus, 845 m).

describe orographic precipitation by a single nondimensional parameter.

The paper is arranged as follows. Section 2 examines orographic precipitation enhancement based on observational data analysis. The numerical model and its setup are described in section 3. Moisture effects on dynamics, especially changes in stability, vertical wavelength, and flow deceleration upstream of the mountain, are discussed in section 4. Section 5 examines the impacts of varying mountain width, flow speed, and stability. A regime diagram for orographic precipitation derived from all available model runs is suggested in section 6. Finally, the results are summarised and discussed in section 7.

## 2 Observations of orographic rainfall

To estimate the magnitude and variability of orographic precipitation, we first examined several real stratiform rain events over different low mountain ranges of Germany. The events considered for this have a duration of at least 24 hours with rain totals in excess of 20 mm over the mountains and a flow direction of ±30° perpendicular to the mountain. The data obtained from synoptic stations of the German Meteorological Service [Deutscher Wetterdienst (DWD)] includes wind speed and direction (10 min average), temperature, dew point temperature, air pressure at station level, present and past weather code (all hourly data), and precipitation sums (6 hours). All data were

accumulated (for R) or averaged over 24-hour periods of time, from which mean wind speed perpendicular to the mountain $U_\perp$, mean static stability $N_d$ in terms of dry Brunt-Väisälä frequency

$$N_d = \sqrt{\frac{g}{\bar{\theta}} \frac{\partial \theta}{\partial z}}, \tag{2.1}$$

with $\theta$ as the potential temperature, and, finally, the Froude number $Fr_d$ were calculated. Since the lifting condensation level (LCL) varied significantly from the lowest levels up to 1.5 km, we decided not to consider the saturated stability $N_m$ (see Eq. 3.4) here.

By multiplying $Fr_d$ with the local incoming horizontal water vapour flux,

$$F'_{wv} = \bar{\rho}_d \bar{r}_v U_\perp, \tag{2.2}$$

where $\rho_d$ and $r_v$ are the density of dry air and water vapour mixing ratio, respectively (the bar indicates the average), and normalising both by their means, we obtain a single precipitation sensitivity parameter $\Psi = \widehat{Fr_d} \times \widehat{F'_{wv}}$. This parameter accounts for both the strength of orographic lifting associated with the flow-over and flow-around regime and the upper limit of moisture that can be converted into precipitation. Precipitation enhancement $\hat{R}$ is expressed by the ratio of rainfall totals between a mountain and an adjacent valley station.

Despite considerable scattering, it is found that $\hat{R}$ is strongly controlled by the precipitation sensitivity parameter $\psi$ over two low mountain ranges shown in Fig. 1. The relations are confirmed by high Pearson correlation coefficients, $r$ = 0.86 for the Black Forest and $r$ = 0.79 for the Thuringian Forest. Similar relationships, but with higher scattering of the data, were also obtained over other low mountain ranges (Harz and Ore Mountains, Rothaargebirge, and Northern Thuringian Forest) (STELLER, 2004). The connection between $\hat{R}$ and the Froude number can be explained by 3D low-level flow going directly over (Fr > 1) or partly around (Fr ∼< 1) the obstacle (e.g. SMITH, 1979; SMOLARKIEWICZ and ROTUNNO, 1989). As $Fr$ increases so do orographically induced vertical motions and precipitation intensities. The relation to $F'_{wv}$, on the other hand, can be explained by the fact that precipitation totals rely strongly on the continuous replacement of humidity after condensation by advection. However, since the orographic precipitation enhancement in Fig. 1 is expressed by the ratio of two stations only, $\hat{R}$ may be sensitive also to the location of the precipitation maximum. Whereas climatologically the maxima are located more or less over the crests with a low sensitivity to the exact position, they may be shifted significantly from one event to another.

# 3 Numerical model

## 3.1 Model description and setup

The idealised, three-dimensional (3D) simulations are performed using the non-hydrostatic limited-area weather prediction model COSMO (Consortium for Smallscale Modeling) developed and applied by the DWD among others. COSMO is based on the fully compressible Navier–Stokes equations using finite differences (SCHÄTTLER and DOMS, 2007; DOMS et al., 2007). This study uses an adjusted version of COSMO 3.19, which is comparable to the subsequent version 4.0, at a horizontal resolution of 2.8 km and 40 vertical layers using a generalised terrain-following coordinate.

A one-and-a-half order turbulence closure, which refers to level 2.5 in the Mellor–Yamada hierarchy (MELLOR and YAMADA, 1982), is applied using a prognostic equation for the turbulent kinetic energy (TKE). Time integration is performed with a 2-time-level 2nd order Runge-Kutta scheme for the dynamics according to WICKER and SKAMAROCK (2002), which provided more realistic results in our idealised setup compared to a 2nd-order Leapfrog scheme. Cloud water condensation and evaporation are calculated by applying a saturation adjustment, and precipitation formation is parameterised by a 5-class microphysics scheme including the species of water vapour, cloud water, cloud ice, rain water, and snow. To consider 3D transport of hydrometeors, the prognostic precipitation scheme was applied. Surface heat and moisture fluxes as well as radiation and the Coriolis force were switched off. The horizontal grid is a rotated latitude/longitude Arakawa C-grid for horizontal differencing of the variables. Boundary conditions are constant according to the initial conditions (inflow boundary) or outflow (all other lateral boundaries) and rigid in *z* with a free-slip lower boundary condition in *u, v,* and *w* and a Rayleigh damping layer above 11 km to minimize spurious reflections of gravity waves from the model top.

The horizontal resolution of 2.8 km allows for turning off the parameterization scheme of deep convection as in the operational mode of COSMO-DE, whereas shallow convection is parameterised using a modified Tiedtke scheme. According to WEISMAN et al. (1997), the major fraction of deep convection with subsequent precipitation can be calculated explicitly by models with resolutions of less than 4 km. This was also demonstrated by BARTHLOTT et al. (in print), who compared five different models with a grid spacing between 1 and 2.8 km, all of them without parameterization of deep convection.

A bell-shaped mountain with circular contours, described by

$$h(x,y) = \frac{H}{\left(\frac{x^2+y^2}{a^2}+1\right)^{1.5}}, \tag{3.1}$$

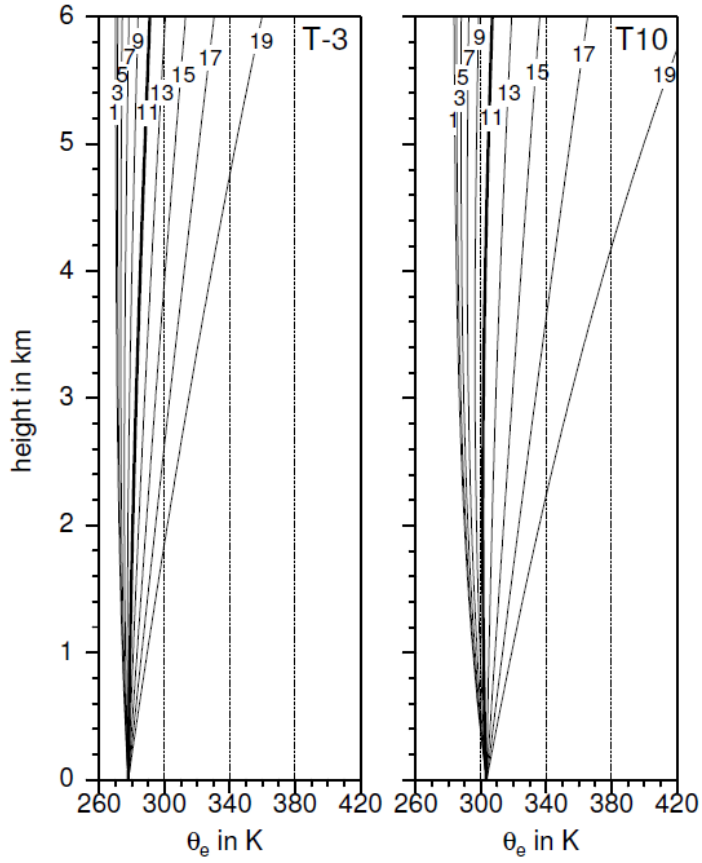


Figure 2: Vertical profiles of $\Theta_e$ (bold: reference profiles) according to BOLTON (1980) for $T_S$ = -3°C (left) and 10°C (right) at different stabilities $N_d$ x $10^{-3}$ $s^{-1}$ indicated in the diagrams (T-3N and T10N in Table 1).

is set in the middle of the domain. The reference terrain profile with a maximum height of $H$ = 1 km and a halfwidth of $a$ = 11 km is roughly based on the dimensions of the Black Forest Mountains located in southwest Germany. In order to prevent spurious reflections of disturbances at the lateral boundaries, the total domain is enlarged in horizontal directions to a size of 553 x 553 $km^2$, which corresponds to 200 x 200 grid points. Extensive test runs revealed that the model setup described above is the most suitable for the idealised simulations performed in this study.

## 3.2 Initialisation

Initial profiles are specified by undisturbed wind speed $U(z) = U$ = const., near-surface temperature $T_s$, and relative humidity $RH(z)$, which is constant up to $z_m$ = 5 km and decreases rapidly above that level according to

$$RH = RH_S \left[0.5 + \frac{1}{\pi}\mathrm{atan}\left(\frac{z - z_m}{500}\right)\right] \tag{3.2}$$

with $RH_S$ as the near-surface humidity. Assuming hydrostatic balance, initialising model temperatures up to 12 km are calculated from constant static stability $N_d$. Beyond this level, the temperature increases according

Kunz, Wassermann: Sensitivity of flow dynamics and orographic precipitation to changing ambient conditions in idealised model simulations
Meteorologische Zeitschrift 2 (2011), S. 199-215. 

| Experiment | RH % | α km | U m $s^{-1}$ | $N_d$ x $10^{-3}s^{-1}$ | $F_{wv}$ kg $m^{-1}s^{-1}$ | $F_{wv}$ kg $m^{-1}s^{-1}$ |
|---|---|---|---|---|---|---|
| T-3R | 95 | 11 | 10 | 11 | 8.28 | 64 |
| T10R | 95 | 11 | 10 | 11 | 4.75 | 176 |
| T-3U | 95 | 11 | 6, 8, 10, 12, 14, 16, 18 | 11 | 8.28 | 38, 51, 64, 77, 90, 103, 115 |
| T10U | 95 | 11 | 6.5, 7.4, 8.5, 10, 12.2, 15.7, 22 | 11 | 4.75 | 114, 130, 149, 176, 215, 277, 388 |
| T-3N | 95 | 11 | 10 | 1.1, 2.9, 5, 7, 9, 11, 13, 15, 17 | -6.1, -5.4, -3.9, 2.5, 5.9, 8.3, 10.4, 12.4, 14.2 | 64 |
| T10N | 95 | 11 | 10 | 1.1, 2.9, 5, 7, 9, 11, 13, 15, 17 | -8.6, -8.2, -7.3, -5.8, -2.9, 4.8, 7.7, 10.2, 12.5 | 176 |
| T10a | 95 | 11, 19, 28, 36, 42, 47, | 20 | 11 | 4.75 | 176 |

| | | | | | | |
|---|---|---|---|---|---|---|
| | | 58 | | | | |
| T10RH | 0, 50, 95 | 11 | 10 | 11 | 4.75 | 176 |

Table 1: Summary of the 3D COSMO model runs performed for this study. The T-3 and T10 in the experiment name refer to the near-surface temperature of $T_S$ = -3°C and 10°C, *R* denote the reference runs, and *U, N, a*, and RH refer to changing wind speed U, Brunt-Väisälä frequency $N_d$, mountain half-width α, and relative humidity *RH*; $F_{wv}$ is the incoming horizontal water vapour flux (Eq. 3.3). Moist static stability $N_m$ (Eq. 3.4) is obtained by averaging $N_m^2$ from the surface up to a level of 5,000 m; negative values indicate instability with imaginary $N_m$.

to the ICAO standard atmosphere. The model is initialised by these profiles as being uniform through the domain.

Ambient conditions were selected to be representative of orographically-dominated widespread precipitation in southwest Germany (KUNZ, 2011). The reference runs are defined by *RH* = 95%, *a* = 11 km, *U* = 10 m s$^{-1}$, and $N_d$ = 0:011 s$^{-1}$. The full list of parameters used to initialise the COSMO model runs is shown in Table 1. Incoming horizontal water vapour flux which may be considered the upper limit of precipitation for stable ascent is quantified by

$$F_{wv} = \int_y \int_z \rho_d r_v U \, dy \, dz \tag{3.3}$$

where *y* is integrated over one grid distance of *Δy*. To account for both summer and winter conditions, two different near-surface temperatures, including $T_S$ = -3°C and 10°C, were used in all runs (hereinafter referred to as T-3 and T10). The sensitivity of orographic precipitation to ambient conditions is investigated by successively changing inflow velocity *U* from 6 to 18 m s$^{-1}$ and static stability $N_d$ from 0.001 to 0.017 s$^{-1}$, whereas the other parameters remain fixed. In order to obtain the same ratio $N_d/U$ over the mountain crest at both temperatures $T_S$, the increments of changing *U* are not constant in the T10 runs.

Release of latent heat of condensation related to lifting above the LCL leads to conditionally unstable layers near the surface in some of the profiles, as can be seen in the decrease of equivalent potential temperature $\Theta_e$ with height (Fig. 2). Therefore, moist stability $N_m$ becomes imaginary for low $N_d$, indicated by negative values in Table 1. Ignoring the falling of hydrometeors and phase changes, $N_m$ is computed by (LALAS and EINAUDI, 1974; DURRAN and KLEMP, 1982)

$$N_m^2 = \frac{g}{T}\left(\frac{\partial T}{\partial z} + \Gamma_m\right)\left(1 + \frac{L r_v}{R_d T}\right) - \frac{g}{1 + r_w}\frac{\partial r_w}{\partial z} \tag{3.4}$$

where $R_d$ is the gas constant for dry air, $r_w$ is the total water mixing ratio, and $L$ is the latent heat of condensation. The moist adiabatic lapse rate $\Gamma_m$ is given by

$$\Gamma_m = \frac{g}{c_p}(1+r_w)\left(1+\frac{Lr_v}{R_dT}\right)\times \left[1+\frac{c_{pv}r_v+c_wr_l}{c_p}+\frac{\epsilon L^2 r_v}{c_pR_dT^2}\left(1+\frac{r_v}{\epsilon}\right)\right]^{-1}, \tag{3.5}$$

where $c_p$, $c_{pv}$, and $c_w$ are the heat capacities of dry air, water vapour, and liquid water in an isobaric process, $r_l$ is the liquid water mixing ratio, and $\epsilon = 0.622$. The initial profiles considered comprise a broad range from moist stable to unstable ascent, where convection-like

Kunz, Wassermann: Sensitivity of flow dynamics and orographic precipitation to changing ambient conditions in idealised model simulations
Meteorologische Zeitschrift 2 (2011), S. 199-215.
S. 204

phenomena may be expected. This allows for detailed examination of the transition between stable and unstable ascent and the relation to the precipitation patterns. Note that the T10 runs tend to be more unstable in the case of saturation due to the higher release of latent heat of condensation.

Different topographies are considered by mountain half-widths varying between 11 and 58 km at T10. The steep 11-km half-width is representative of the southern Black Forest (SW Germany), while the medium 28-km width represents several low mountain ranges, such as the Thuringian Forest, Ore Mountains (both East Germany), or Harz Mountains (Central Germany). Finally, the 56-km width is similar to very broad mountains such as the Rothaargebirge (West Germany). Mountain height was not changed, since it is approximately valid for several low mountain ranges.

Despite slight numerical instabilities, nearly steadystate conditions are reached after four hours of integration time. Thus, precipitation discussed below is obtained by the difference of temporally accumulated precipitation between $t = 5$ h and 4 h simulation time. Under moist unstable conditions, the simulation results did not reach the steady state due to convective development. For reasons of consistency, however, we always used the same model time to quantify the precipitation totals.

## 4 Moisture effects on dynamics

In a stably stratified atmosphere, forced vertical displacement of the air going over a mountain creates restoring forces that initiate atmospheric gravity waves. In the case of vertically propagating

waves, the vertical wind speed oscillates up and down, leading successively to saturated and unsaturated regions. While lifting leads to cooling and condensation beyond the LCL, descent is associated with warming and drying, where rain drops or ice particles may evaporate or melt, respectively. Assuming moist adiabatic vertical motions, latent heat of condensation (evaporation) is released or absorbed due to phase transitions. To consider the effect of saturated flows, a moist stability concept was suggested by various authors (e.g., FRASER et al., 1973; DURRAN and KLEMP, 1982; JIANG, 2003; KUNZ and KOTTMEIER, 2006b). In this concept, the dry Brunt-Väisälä frequency $N_d$ is substituted by the saturated equivalent $N_m$ in the linear wave equations and, consequently, in the moist nondimensional mountain height $M_m = Fr_m^{-1}$.

## 4.1 Changes in static stability during mountain overflow

Flowing over a mountain, an initial temperature profile is modified by both vertical motions and phase transitions. Assuming dry adiabatic motions, lifting tends to reduce static stability, while the opposite applies to descent. This effect is much more pronounced within a saturated environment and pseudo-adiabatic motions.

Modifications in static stability are illustrated in Fig. 3 that shows deviations of the initial $N_d$ and $N_m$ profiles at four positions on the centre line through the mountain under both dry (RH = 0%) and almost saturated (RH = 95%) conditions from the T10R experiments (cf. Table 1). In general, the profiles from the two model runs are quite similar with stronger deviations being restricted to the crest and downstream. Consideration of $N_m$ yields deviations in the same direction as $N_d$, but with a higher magnitude. In the region of slight orographic lifting upstream of the crest (Fig. 3a), a shallow layer with reduced stability develops. In the RH95 experiment, this layer is even slightly unstable. On the other hand, descent at a height between 2 and 4 km tends to increase static stability. In the region of strong descent over the crest (Fig. 3b), stability increases further up to a level of 3 km.

The absorption of latent heat due to evaporation over and downstream of the crest reduces the stabilising effect of the descent. Ascent related to the gravity wave aloft (see Fig. 4) is reflected by further decrease in both $N_d$ and $N_m$, but the zero-crossing of RH95 is shifted vertically by about 500 m compared to the RH0 run due to the increase in the vertical wave length within a saturated environment, as will be discussed in the next section. Downstream of the crest (Figs. 3c and d) the profiles of $N_d$ are almost similar for RH0 and RH95, still showing the vertical shift. The strong deviation of $N_m$ from the initial profile is due to higher velocities associated with the gravity wave (cf. Fig. 4), leading to enhanced latent heat transfer. Whereas slight ascent beneath 1.500 m causes a slight decrease in stability at the grid point far downstream (Fig. 3d), evaporation tends to stabilise the stratification just a few 100 m above the surface.

## 4.2 Gravity waves and their vertical wavelengths

The tendency of the flow to go over or around an obstacle can be described by the Froude number or its inverse, the nondimensional mountain height $M = Fr^{-1}$ (SMOLARKIEWICZ and ROTUNNO, 1989). Adding additional moisture until almost saturation (RH = 95%) results in more direct overflow of the mountain due to reduced stability and, thus, a lower $M$. This overflow coincides with a steepening and weakening of the gravity waves, as can be seen in the cross-sections of the vertical velocity with the typical periodic pattern of ascent and descent regions and the upstream tilt of the phase lines (Fig. 4b).

Over a wide mountain and/or high stability and/or for weak wind speed, buoyancy forces become dominant and vertical accelerations are so weak that the flow can be considered to be hydrostatic. This is the case when

Kunz, Wassermann: Sensitivity of flow dynamics and orographic precipitation to changing ambient conditions in idealised model simulations
Meteorologische Zeitschrift 2 (2011), S. 199-215.
S. 205

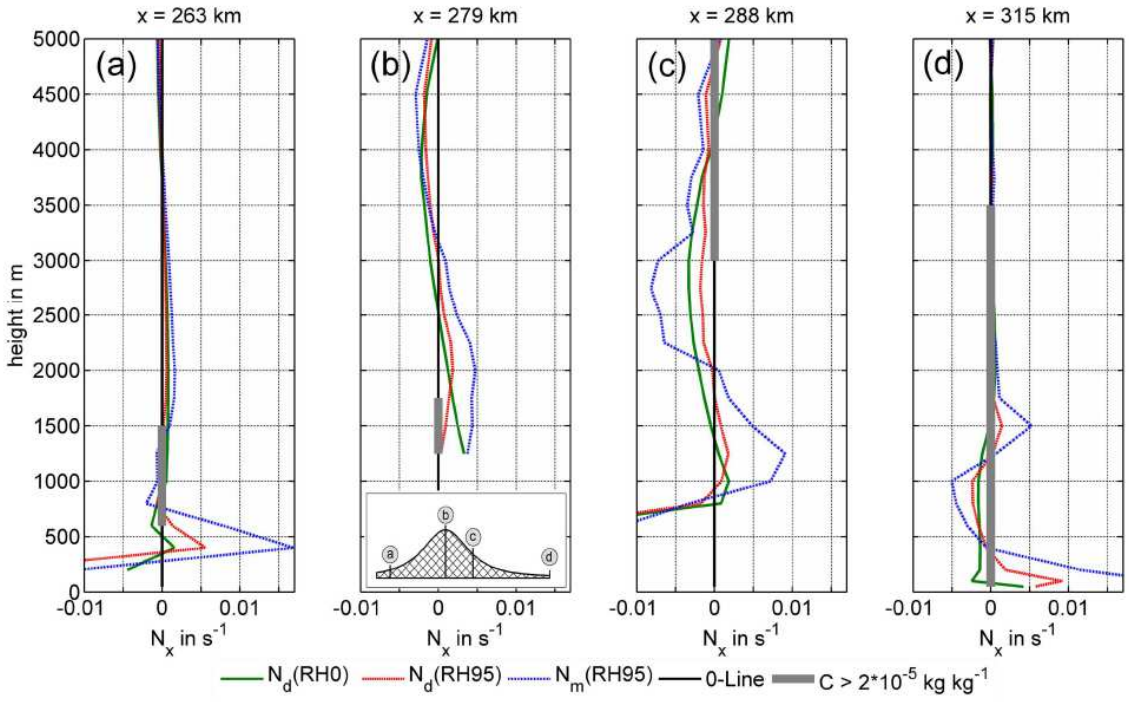


Figure 3: Deviations of the vertical profiles of $N_d$ and $N_m$ compared to the initial profile of $N_d$ = 0.011 $s^{-1}$ = const. at four locations through the centre line of the domain for unsaturated (RH = 0%; green line) and saturated flow over the mountains (RH = 95%; red and blue lines). The locations (a-d) are shown in the small subfigure. The vertical bold grey lines

at x = 0 indicate saturation, where $N_m$ should be used instead of $N_d$. Other parameters are according to T10RH in Table 1.

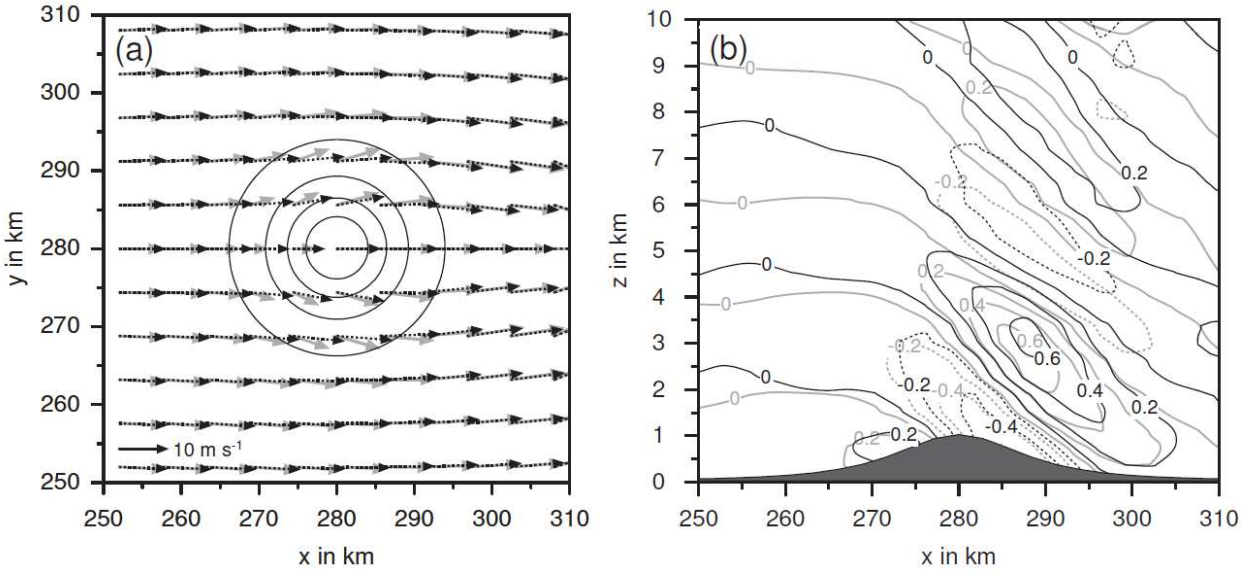


Figure 4: Horizontal (lowest model level) and vertical cross-sections of horizontal (a) and vertical (b) wind speed from T10RH experiments for unsaturated (RH = 50%; grey lines) and saturated (RH = 95%; black lines) flow over the mountain (orography in 200 m intervals in a).

the nondimensional mountain width

$$M_a = \frac{aN_d}{U} \ll 1 \tag{4.1}$$

In this limit, non-dispersive, vertically propagating waves develop and the vertical wavelength is given by

$$L_z = \frac{2\pi U}{N} \tag{4.2}$$

In the T10RH runs, the parameter $M_a$ is 12.1 (RH50) and 5.3 (RH95), indicating that the flow is approxi-

Kunz, Wassermann: Sensitivity of flow dynamics and orographic precipitation to changing ambient conditions in idealised model simulations
Meteorologische Zeitschrift 2 (2011), S. 199-215. 

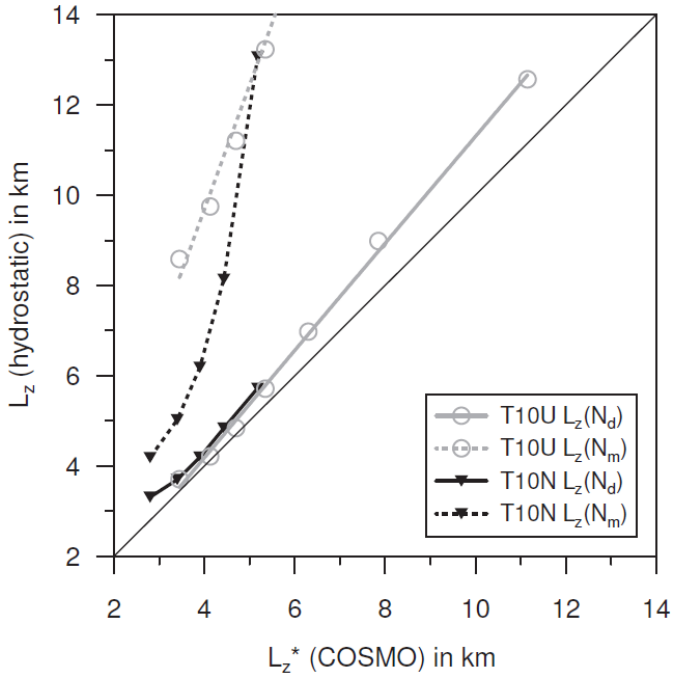


Figure 5: Vertical wavelengths estimated from the T10N and T10U simulations ($L_z^*$ on the x-axis) and quantified from the inflow parameters using Eq. (4.2) ($L_z$ on the y-axis) for $N_d$ (solid lines) and $N_m$ (dashed lines). Each point in the diagram represents a single COSMO run; the solid thin line is the 1:1 divide. Only results with a positive $N_m$ are shown.

mately hydrostatic. The vertical wavelength without saturation is $L_z$ = 5.7 km according to (4.2). From the COSMO simulation displayed in Fig. 4b, the wavelength can be estimated to as $L_z^* \approx$ 4.5 km, which is near to the value quantified by (4.2). The underestimation presumably is due to an increase in stability in the lower layers over and downstream of the mountain, associated with net descent (cf. Fig. 3).

Substituting $N_d$ (= 0.011 $s^{-1}$) by $N_m$ (= 0.0048 $s^{-1}$) for the saturated case (RH95) gives $L_z$ = 13.2 km, which is far above $L_z^* \approx$ 5:5 km estimated from the COSMO simulation. This discrepancy above all is due to the wave pattern over the mountain with oscillating vertical motions and, thus, saturated and unsaturated regions as indicated in the vertical profiles of Fig. 3. Apparently, it does not only occur in the two experiments discussed, but in all COSMO runs performed. Fig. 5 shows vertical wavelengths quantified by (4.2) and estimated from the COSMO simulations, $L_z$ and $L_z^*$ , respective-

ly, based on the T10U and T10N runs. It is obvious that $L_z^*$ is much closer to the analytical solution when considering $N_d$ instead of $N_m$. In particular for changing $U$, the results differ largely. For very low dry stability $N_d$, the corresponding $N_m$ becomes imaginary and $L_z$ remains undefined. The results obtained from the T-3 experiments are qualitatively the same, but the spread between the two pairs of curves is lower due to reduced release of condensation heat (not shown).

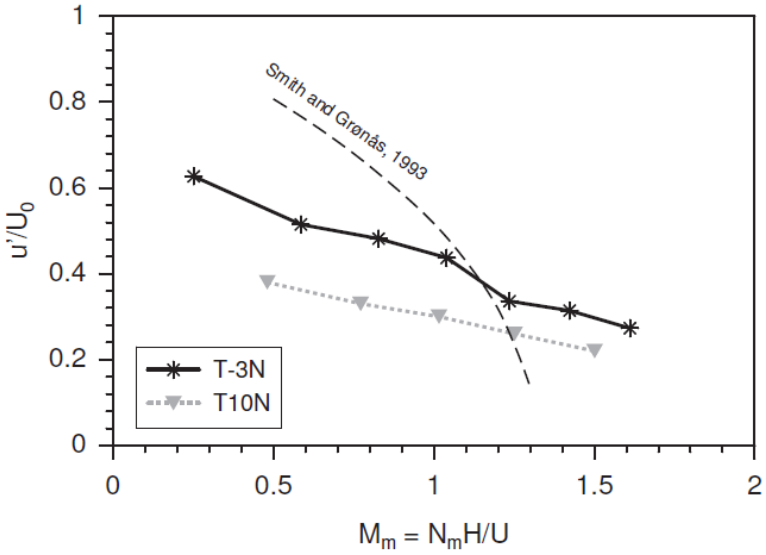


Figure 6: Flow deceleration according to SMITH and GRØNÅS (1993) and from T-3N (solid black line) and T10N (dashed grey line) COSMO experiments with changing stability $N_d$.

## 4.3 Flow deceleration upstream of the mountain

Under dry conditions, the onset of flow stagnation is controlled by a critical nondimensional mountain height, $M_c$ (or critical Froude number, $Fr_c$). Following Sheppard's law (SHEPPARD, 1956) which is based on the energy transformation argument from kinetic into potential energy, $M_c$ = 1 for windward stagnation regardless of the mountain shape. This reasoning, however, ignores the pressure difference term, which can be of the same magnitude or even larger than the kinetic energy term. Flow deceleration curves produced by SMITH and GRØNÅS (1993) with a numerical model suggest a higher value for $M_c$ compared to Sheppard's law. In a later study, JIANG (2003) reproduced these curves with the Advanced Regional Prediction System (ARPS) model and found a value of $M_c$ = 1.32.

For incoming saturated flows it is expected that latent heat release delays the onset of stagnation on the windward slope (and also on the lee-side, which is not examined here). Fig. 6 shows the flow deceleration upstream of the mountain in terms of minimum wind speed $u'$ = Min($u(x; y \leq 280$ km, $z \leq 1$ km)) determined from the COSMO runs with changing $N_d$. To obtain a quantity comparable with previous works, $u'$ is normalised by the undisturbed wind speed $U$ (= 10 m s$^{-1}$) and displayed

as a function of the saturated nondimensional mountain height $M_m$. Values for unstable conditions ($N_m^2 < 0$) were omitted because of non-stationary. Compared to the results of SMITH and GRØNÅS (1993) for dry conditions, the two curves for T-3N and T10N exhibit a significantly weaker slope suggesting that inclusion of moisture reduces flow stagnation. Within the parameter range considered, stagnation does not occur at both temperatures. However, the simulation results suggest that the saturated flow is less decelerated for higher values of $M_m$ (or $N_m$) compared to the dry solution.

Kunz, Wassermann: Sensitivity of flow dynamics and orographic precipitation to changing ambient conditions in idealised model simulations S. 207
Meteorologische Zeitschrift 2 (2011), S. 199-215.

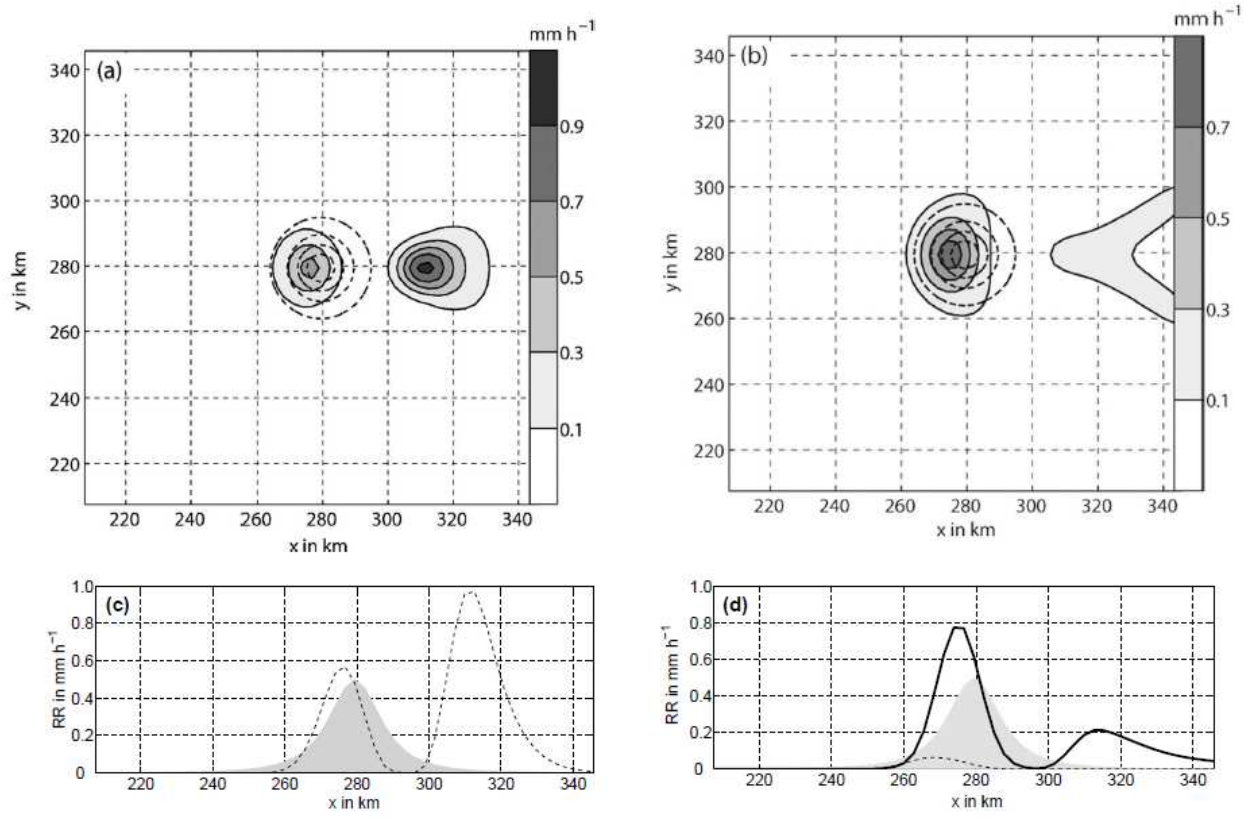


Figure 7: Precipitation intensity on the ground as horizontal cross-sections (a, b) and on the centre line with rain (thin line), snow (thick line), and orography (H = 1 km; shading) (c, d) after 5 h of simulation time from T10R (a, c) and T-3R (b, d).

This delay can be understood qualitatively by considering the moist stability concept. This approach is reasonable since flow stagnation upstream of the mountain occurs in a saturated environment due to stable ascent in the lowest layers (cf. Fig. 3), which is not the case when describing

gravity waves as shown in the previous section. Similar results were also obtained by JIANG (2003), but only for changing mountain heights. He demonstrated that the dry and moist deceleration curves are comparable when estimating $N_m$ properly from the background flow, yielding $M_c \approx 3$. The study, however, shows also different results for different stabilities. Besides, while our simulations were performed for bell-shaped mountain profile, the studies of SMITH and GRØNÅS (1993) and JIANG (2003) are based on a Gaussian-shaped obstacle. The more gently sloped bellshape mountain can lead to a delayed onset of windward stagnation and to some differences in the absolute values (BAUER et al., 2000), which may explain some of the discrepancies.

In our work flow stagnation does not occur within the parameter range applied. Even if the results were obtained from highly idealised model simulation, this may imply that flow stagnation is of no major relevance to typical frontal precipitation events over low-mountain ranges with a characteristic mountain height of 1000 m (or below). This hypothesis is supported by the fact that wind speeds near zero were never observed at one of the valley stations during significant orographic precipitation events (cf. Sec. 2).

## 5 Impact of changing parameters on orographic precipitation

After the discussion of flow modifications due to vertical motions and related diabatic effects, the intention of this section is to explore how ambient conditions and mountain characteristics change orographic precipitation patterns. The sensitivity of orographic precipitation is investigated by a set of COSMO simulations, where one of the parameters $a$, $U$, and $N_d$ is successively altered, whereas the others are kept fixed according to the reference runs T-3R and T10R.

### 5.1 The reference runs T10R and T-3R

The sensitivity study will be started by discussing the two reference experiments, T10R and T-3R (see Table 1 and profiles in Fig. 2). Both cases are characterised by the same nondimensional mountain height of M = 1.1 (Fr = 0.91). The simulated precipitation patterns, however, significantly differ from each other. While maximum totals are approximately the same, the T10R run

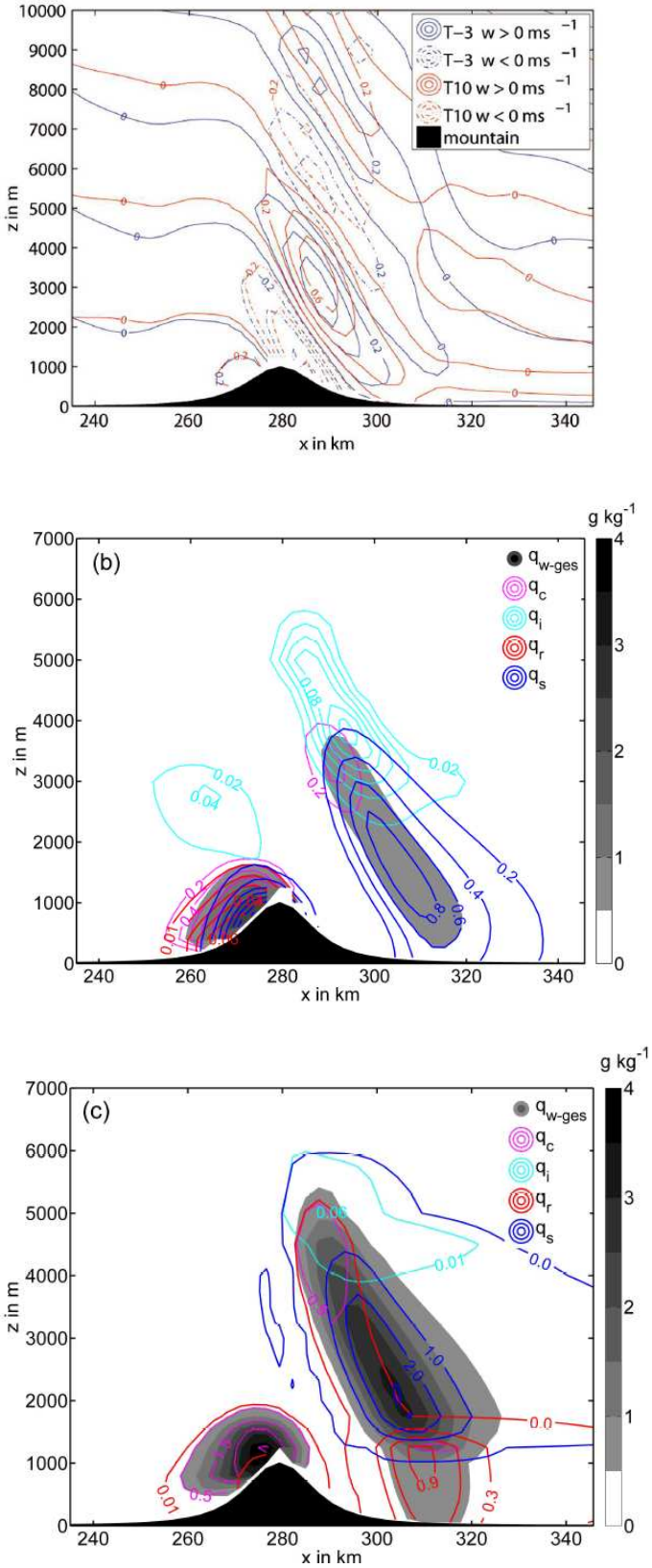


Figure 8: Vertical cross-sections through the centre line of the domain for the reference runs with vertical wind speed w (a) and specific contents (in $10^{-4}$ g $kg^{-1}$) of total water $q_w$

(shading), cloud water $q_c$, cloud ice $q_i$, rain $q_r$, and snow $q_s$ (isolines) for T-3R (b) and T10R (c).

produces most precipitation downstream of the mountain (Figs. 7a and c). In the T-3R experiment, most of the precipitation falls upstream and over the mountain and only weak precipitation downstream (Figs. 7b and d).

In both cases, strongest lifting occurs downstream of the crest associated with the gravity wave (Fig. 8a). Whereas the mean vertical velocity of the first wave up-

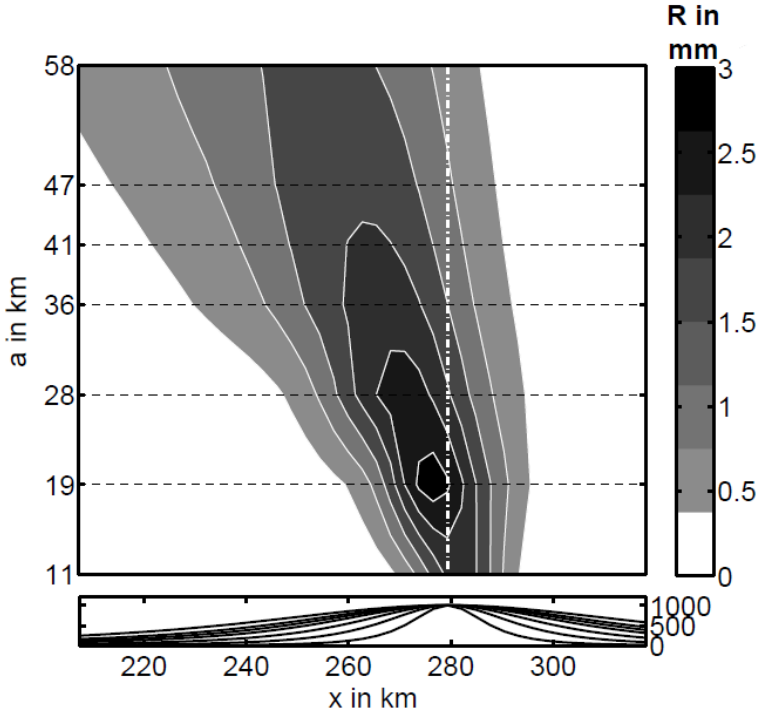


Figure 9: Sensitivity of surface precipitation through the centre line of the domain accumulated over one hour to changing mountain a; other parameters are according to T10a (see Table 1). The dashed horizontal lines represent the simulation results for the half-width a indicated; the values in-between are linearly interpolated.

stream is approximately the same, both the descent and the second ascent downstream of the mountain exhibit higher magnitudes in T10R compared to T-3R. As already discussed in the previous section, this is due to a higher release of condensation heat in T10R. The resulting increase in the vertical wavelength leads to a spatial extension of the gravity waves which are also shifted further downstream in T10R. The varying dynamics solely, however, cannot explain the different precipitation patterns obtained by the two runs.

Despite the low temperature, a mixed-phase cloud, which consists of cloud water and cloud ice, forms upstream of the mountain in the T-3R run (Fig. 8b). Accretion and riming in the low-level cloud lead to a short delay between lifting and precipitation fallout. Related cloud water conversion time scales of $\tau_c \approx 500$ s are lower than the time scale for mountain overflow, which can be estimated by $\tau_m = a/U = 1100$ s. Consequently, most of the precipitation reaches the ground upstream of the crest. If the time scales for cloud conversion and hydrometeor fallout, $\tau_c$ and $\tau_f$, are too long, condensate and hydrometeors would be advected downstream of the mountain where they may evaporate in descent regions without precipitation reaching the ground. On this side, a vertically extended ice cloud associated with the gravity wave forms. Ice and snow particles with slow terminal fall velocities are advected over larger distances and partly evaporate when entering descent areas.

In the T10R run, a warm cloud forms upstream of the mountain (Fig. 8c). Since characteristic time scales for autoconversion and accretion are significantly higher than those in a mixed-phase cloud, most of the hydro-

Kunz, Wassermann: Sensitivity of flow dynamics and orographic precipitation to changing ambient conditions in idealised model simulations
Meteorologische Zeitschrift 2 (2011), S. 199-215.
S. 209

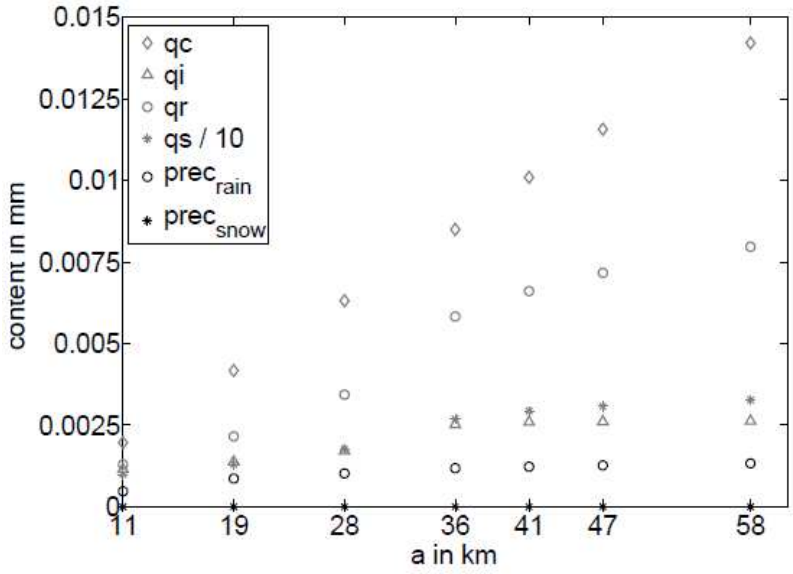


Figure 10: Area-averaged accumulated precipitation (black dots) and cloud components (grey dots) for different mountain half-widths a of the T10a experiments; $prec_{rain}$ and $prec_{snow}$ are rain and snow on the ground.

meteors are advected into descent regions downstream. Due to the higher incoming water vapour flux in the T10R case of $F_{wv}$ = 176:1 kg m$^{-1}$ s$^{-1}$ compared to 64 kg m$^{-1}$ s$^{-1}$ in T-3R, a dense cloud aloft with high amounts of specific cloud ice $q_i$ forms downstream. Even if evaporation substantially reduces specific rain and snow content $q_r$ and $q_s$, high amounts of rain still reach the ground.

In conclusion, the different precipitation patterns of T-3R and T10R in Fig. 7 are a result of the interaction of flow dynamics and microphysics. This finding is important for understanding the variable precipitation patterns which will be discussed in the next sections.

## 5.2 Impact of mountain half-width

It is now evaluated how variations in the mountain half-width a change both orographic precipitation and cloud microphysics. To confine to mountain barrier effects only, ambient conditions are specified according to mountain overflow ($M$ = 0.44; $Fr_d$ = 2:3) by $U$ = 20 m s$^{-1}$, $N_d$ = 0.011 s$^{-1}$, and $T_S$ = 10°C (T10a in Table 1).

Fig. 9 shows the corresponding precipitation totals through the centre line of the model domain. Each of the horizontal lines indicates a single COSMO simulation. Values between the lines are linearly interpolated for the sake of readability. With increasing mountain width, orographic precipitation is stretched horizontally, while maximum intensity upstream of the mountain decreases from 2.5 to 1.3 mm. Total precipitation accumulated over the whole domain increases as well, but very slowly (Fig. 10). At the same time, the maxima are shifted further upstream, from a location near the crest at a = 11 km to approximately 20 km upstream at a = 59 km. Over the broadest mountain, the precipitation area expands up to 80 km in upstream direction.

Spillover downstream of the mountain is found to be almost insensitive to variations in the mountain width a. The time scale for mountain overflow $\tau_m$ is in the range of the cloud conversion and fallout time scales ($\tau_c$+$\tau_f$ ∼ 500 s) when precipitation is from rain only (cf. Fig. 10). Thus, despite the high wind speed of 20 m s$^{-1}$, only a minor amount of hydrometeors is advected downstream, in particular over the broader mountains. This is different in the cold cases of T-3, where the precipitation maxima, consisting of snow only with higher time scale for fall-out $\tau_f$ , are shifted further downstream (not shown). With increasing half-width $a$, spillover decreases and the maxima are found upstream of the mountain in accordance to the study of JIANG and SMITH (2003).

The amounts of $q_c$ integrated vertically and horizontally over the domain exceed that of $q_i$ by a factor between 1.5 and 2 in the T10a experiments (Fig. 10). Precipitation on the ground, however, consists of rain solely. As the mountain width increases, so do the cloud components $q_c$ and $q_i$, but not the specific rain water and snow contents, $q_r$ and $q_s$. Both quantities slightly increase up to a mountain half-width of $a$ = 36 km and remain approximately constant afterwards. Surface precipitation is directly related to these quantities, meaning that evaporation of hydrometeors is of minor importance since most of the precipitation falls to the ground upstream of the mountain. The opposite trend between condensate and precipitation indicates that precipitation efficiency defined as total precipitation normalised by condensation is highest for steep mountains and successively decreases with mountain width.

## 5.3 Impact of wind speed

In order to understand how orographic precipitation responds to the changes in the flow charateristics, we first varied wind speed between 6 and 18 m $s^{-1}$, while the static stability of $N_d$ = 0.011$s^{-1}$ remained constant (T-3U and T10U experiments in Table 1). The nondimensional mountain height $M$ is between 0.5 and 1.8 (corresponding to $Fr$ between 2 and 0.55), indicating a transition from partly blocked to the unblocked flow regime.

At both temperatures, two precipitation areas develop (Fig. 11) in association with the gravity waves discussed in the previous section. With increasing wind speed, upstream precipitation increases almost linearly, whereas the secondary maximum weakens and, finally, vanishes. Additionally, the precipitation areas are broadened and their maximum is shifted further downstream due to increasing advection of hydrometeors. In the T10 case at higher wind speeds, the maximum occurs a bit downstream of the crest, while it is slightly shifted upstream in the T-3 run. For $U$ > 10 m $s^{-1}$ (M = 1.1, Fr = 0.91), most of the precipitation falls upstream of or over the crest at T10. Higher penetration of the mountain wave together with the flow more directed over the

Kunz, Wassermann: Sensitivity of flow dynamics and orographic precipitation to changing ambient conditions in idealised model simulations
Meteorologische Zeitschrift 2 (2011), S. 199-215.
S. 210

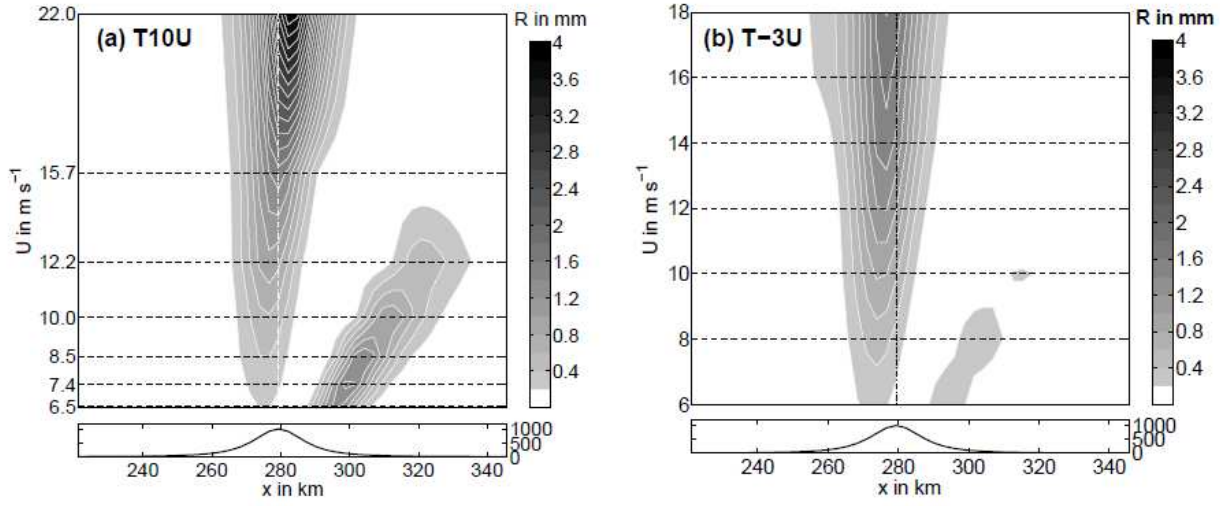


Figure 11: Same as Fig. 9, but for variable U; other parameters are according to T-3U and T10U.

mountain leads to this intensification of upstream precipitation.

Since upstream flow deceleration or stagnation is associated with flow around the mountain, this effect can be quantified by the deflection ratio, DFR, according to KIRSHBAUM and SMITH (2008):

$$DFR = \frac{1}{\delta y F_{wv}} \int_0^{x_c} \int_z \left(\rho_d q_t v|_{y2} - \rho_d q_t v|_{y1}\right)\, dz\, dx, \tag{5.1}$$

where $q_t$ is the total specific water content, $x_c$ = 280 km defines the middle of the domain, and $\delta y$ = $y_2$ -$y_1$ (10 grid points) with $y_1$ = 266 km and $y_2$ = 294 km, which is twice the mountain half-width plus one grid point at both sides. Without normalising by $F_{wv}$, Eq. (5.1) defines the horizontal moisture flux divergence.

With increasing flow speed $U$ the deflection ratio DFR decreases as can be seen in Fig. 12 for the T10 runs. A similar result is found for the T-3 runs which exhibit slightly enhanced DFR due to lower release of condensation heat (not shown). As $U$ increases from 6.5 to 10 m $s^{-1}$, DFR shows the strongest decrease from 31.8 to 24.8%. In this regime with $M > 1$, a higher fraction of the incident moisture detours around the mountain. The extended gravity wave produces significant precipitation which dominates total precipitation in T10U. For $M < 1$, DFR is not very sensitive to a further increase in $U$.

To determine the fraction of moisture removed from the atmosphere by precipitation, total precipitation $R$ is normalised by $F_{wv}$ to obtain the drying ratio (DR). According to SMITH et al. (2005), DR expresses the conversion of the upstream moisture flux into precipitation:

$$DR = \frac{R}{F_{wv}} = \frac{\int_{x_1}^{x_2} R(x)\, dx}{\int_{z_1=0}^{z_2} \rho_d r_v U\, dz} \tag{5.2}$$

Here, precipitation $R$ is integrated from $x_1$ = 238 km to $x_2$ = 322 km in order to capture the totals around the mountain, and $F_{wv}$ is integrated from the surface $z_1$ = 0 m to a maximum height of $z_2$ = 10 km.

Fig. 12 shows that DR is much higher in the colder air over the whole range displayed indicating that a higher fraction of moisture is removed from the impinging air mass as orographic precipitation. As discussed by KIRSHBAUM and SMITH (2008), the inverse dependence of DR on $T_S$ results from the negative slope of $d \ln e_{sat}/dT$ in the Clausius-Clapeyron equation. Besides, there is also a component that comes purely from cloud microphysics. Accretion and riming in a mixed-phase microphysical process is much more efficient compared to the warm-phase autoconversion in a Kessler-type scheme (SEIFERT and BEHENG, 2006). The flow-around cases for $U < 10$ m $s^{-1}$ are associated with higher values of *DR*. After this point, *DR* shows a slight increase in T10U or marginal variations in T-3U runs only.

For comparison, Fig. 12 also shows results obtained from a simple diagnostic model for orographic precipitation according to SMITH and BARSTAD (2004). This model solves the linearised equations of stratified non-hydrostatic flow over mountains (SMITH, 1980) in Fourier space and considers advection of the vertically integrated cloud water content and hydrometeors by characteristic time

scales for cloud water conversion ($\tau_c$ = 1000 s) and fallout ($\tau_f$ = 800 s). In both cases, the COSMO results are similar to the linear solution, as long as $U \geq 10$ m s$^{-1}$. The discrepancy between the two models at lower $U$ is an indication of non-linear effects determining flow characteristics and resulting precipitation areas.

## 5.4 Impact of static stability

Finally, we investigated how changes in static stability modify orographic precipitation and under which

Kunz, Wassermann: Sensitivity of flow dynamics and orographic precipitation to changing ambient conditions in idealised model simulations
Meteorologische Zeitschrift 2 (2011), S. 199-215. 

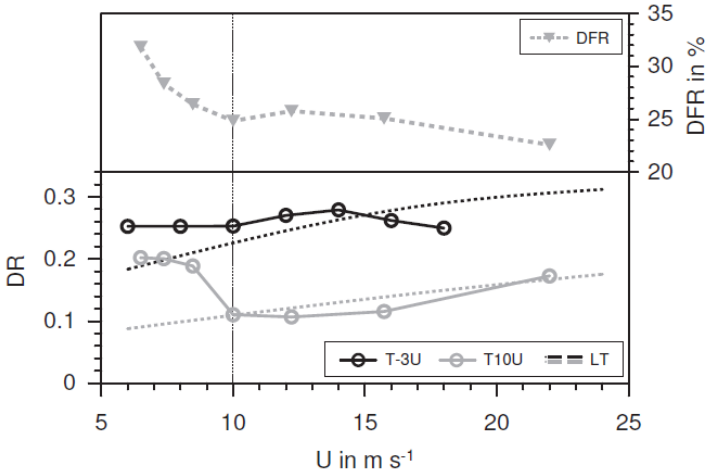


Figure 12: Deflection ratio DFR (dotted line) and drying ratio DR according to the COSMO experiments T-3U and T10U (solid lines) and from linear theory (dashed lines). See text for further explanations.

conditions convection-like patterns emerge. Model runs were performed with varying static stability $N_d$ between 0.0011 and 0.017 s$^{-1}$ with increments of 0.002 s$^{-1}$ both for T-3 and T10 (see T-3N and T10N experiments in Table 1). The corresponding nondimensional mountain height M is between 1.7 and 0.11 (Fr between 0.59 and 9.1), indicating partly blocked flow right up to direct overflow as it was the case for changing wind speeds in the previous section.

Because $M_d$ is inversely proportional to $N_d$, the y-axis in Fig. 13, which shows orographic precipitation along the centre line for changing $N_d$, goes from large to small values. The relation $N_d$ vs. $R$, however, is not as clear as it was found for changing flow speed $U$, because several unexpected de-

tails occur at first sight. In general, the decrease in $N_d$ causes an increase in the precipitation totals, but also a change in the location of the maxima. As long as the stratification is very stable ($N_d \geq 0.011$ s$^{-1}$), two precipitation areas develop, but with higher amounts downstream of the mountain. In this range, the spatial distributions of the T-3N and T10N experiments are almost similar and primarily controlled by the gravity waves downstream.

In the T-3N experiments, the location of the maxima shifts from the downstream to the upstream side of the mountain at $N_d \approx 0.011$ s$^{-1}$ ($M = 1.1$), where the flow regime changes from flow around to flow over the mountain. As already discussed in the previous section, a mixed-phase cloud forms upstream, causing the higher amounts of precipitation. Further decrease in $N_d$ causes further increase in upstream precipitation. The shift in the location of the maxima, however, is not found in the T10N experiments, where a broad rainband develops downstream for $N_d \leq 0.009$ s$^{-1}$.

Further decrease in $N_d$ causes non-stationary structures downstream as well as upstream of the mountain in both cases. In the T-3N runs, the transition to the irregular patterns occurs at $N_d \leq 0.007$ s$^{-1}$, whereas it already starts at $N_d \leq 0.009$ s$^{-1}$ in the T10N runs. The corresponding saturated stabilities $N_m$ are 0.0025 s$^{-1}$ and -0.0029 s$^{-1}$, respectively (note that the negative sign indicates imaginary $N_m$). Even if in the T-3N case the conditions are still slightly stable, it is obvious that the transition from regular stable-ascent precipitation patterns to irregular convection-like patterns is controlled by $N_m$ rather than by $N_d$.

To further scrutinise the transition of the precipitation patterns, we performed additional COSMO experiments in this range with increments of $\Delta N_d = 0.0001$ s$^{-1}$ (not shown). It turned out that the broad precipitation area downstream in the T10N cases develops more or less abruptly and remains persistent with only slight changes afterwards. In contrast to this, downstream precipitation in the T-3N experiments starts slowly and stays comparatively weak. The differences in the precipitation fields and in the onset of convection between the two simulation sets are primarily due to the release of latent heat that destabilises atmospheric stratification. In the T-3N runs, less available water vapour and higher precipitation efficiency upstream of the mountain keep instability effects weak and restricted to the area downstream of the mountain crest. This is consistent with the findings of other authors like KIRSHBAUM and DURRAN (2004) or FUHRER and SCHÄR (2005), who showed that $N_m < 0$ is a necessary but insufficient condition for the onset of embedded convection. Based on a set of 3D idealised simulations, FUHRER and SCHÄR (2005) found that embedded convection is strongly sensitive to the presence of (random) perturbations in the upstream profile. Besides, uniform upstream flow acted to inhibit the cellularity. The transition from purely stratiform to convective precipitation may also occur in a slightly stable environment as the development of unstable regions is affected by the flow dynamics. Therefore, the onset of embedded convection may change depending on the actual vertical profile.

## 6 Regime diagram for orographic precipitation

Finally, of particular interest is the question to what extent the magnitude and location of orographic precipitation can be described by the nondimensional mountain height $M_m$, regardless of whether

$U$ or $N_m$ was varied. To obtain a quantity independent of the moisture load, we considered the drying ratio $DR$ (Eq. 5.2) instead of precipitation totals in these relations. Due to the scaling with the moisture flux $F_{wv}$, $DR$ is less sensitive to variations in wind speed. The relation $DR$ vs. saturated nondimensional mountain height $M_m$ is shown in Fig. 14 (upper part) for all COSMO model runs with variable static stability $N_d$, wind speed $U$, and near-surface temperature $T_S$.

Kunz, Wassermann: Sensitivity of flow dynamics and orographic precipitation to changing ambient conditions in idealised model simulations
Meteorologische Zeitschrift 2 (2011), S. 199-215.


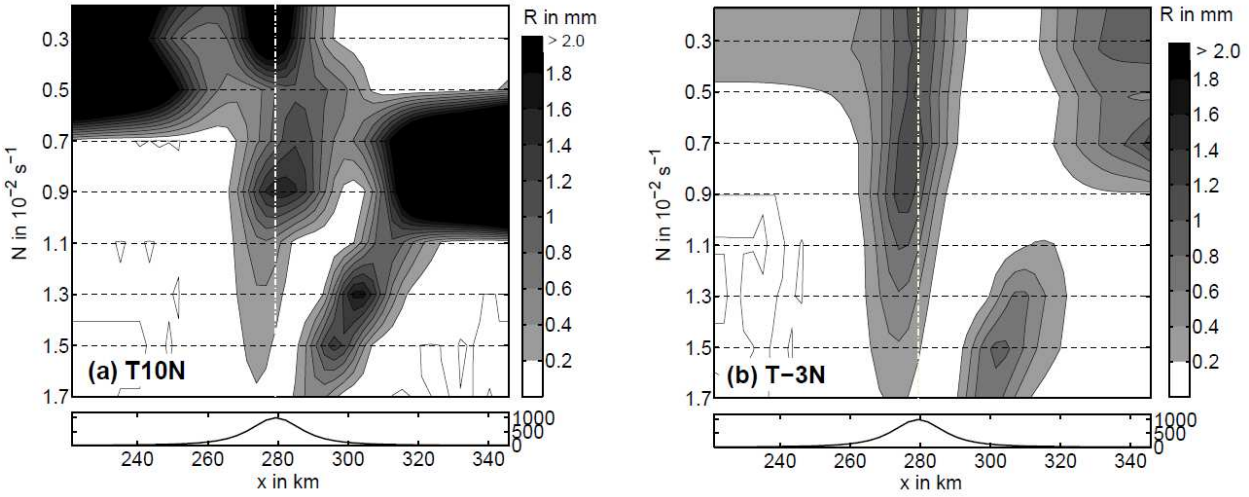


Figure 13: Same as Fig. 9, but for variable $N_d$; other parameters are according to T-3N and T10N.

As long as the flow is stably stratified ($M_m^2 > 0$), $DR$ is not very sensitive to changes of $M_m$, in particular at the lower temperature of T-3, where the regression line is almost horizontal and the confidence intervals are very narrow (90% level of significance). In the mean, $DR$ = 0.26±0.028 (± standard deviation) when neglecting the outlier at $M_m$ = 0.25. In the T10 experiments, $DR$ = 0.14 ± 0.054, indicating not only significantly lower values, but also a higher variability. The increased scatter of the T10 data can be ascribed to changes in the location of the precipitation maxima, which significantly modify $DR$. As already discussed in the previous section, the systematic differences between T-3 and T10 can be explained by the stronger dependency of $F_{wv}$ to changes in the temperature compared to $R$. The most interesting result, however, is that despite the scatter of the data points, $DR$ values obtained from changing $U$ are approximately the same as for changing $N_m$, at least in the T-3 cases. This means that the ratio $N_m/U$ can be considered a controlling parameter for orographic precipitation. Besides, it also confirms the finding of the relation between $\hat{R}$ and the precipitation sensitivity $\psi$ derived from observational data (cf. Fig. 1).

Considering the ratio between upstream and downstream precipitation in the T-3 experiments (lower part of Fig. 14), the results of the experiments approximately collapse on two different exponentially increasing curves, depending on whether *N* or *U* was varied. The transition between the precipitation regimes occurs at a nondimensional mountain height of $M_m \approx 0.95$ (T-3N) and $M_m \approx 1.2$ (T-3U), respectively. For $M_m \geq 1.2$, implemented by higher stability or lower wind speed, downstream precipitation dominates total precipitation up to a factor of four. This statement, however, must be restricted to the colder T-3 cases since the precipitation maxima of the T10 runs are more or less restricted at a position downstream of the mountain for changing $N_d$ (cf. Fig. 13a). Besides, the differences reveal that moist flow dynamics and related orographic precipitation can be fully ascribed neither to $M_m$ ($N_m$) nor to $M_d$ ($N_d$).

In the unstable regime, where $M_m^2 < 0$ (negative range of $M_m$ in Fig. 14), precipitation is dominated by embedded convection rather than terrain-induced precipitation due to the significantly higher vertical wind speeds. Therefore, the results do not show any relation between $M_m$ and *DR* or the location of the precipitation maxima. In this range, however, the maxima are restricted to a downstream position (T-3N). Embedded convection is highly unsteady, and precipitation may temporarily exceed $F_{wv}$. This explains both the apparently random behaviour of *DR* and the high values of up to 110% when Mm becomes imaginary. It is obvious that during stable ascent conditions ($M_m > 0$) *DR* cannot exceed $F_{wv}$ as it is also confirmed by the values below 40%.

## 7 Summary and conclusions

Mountain barriers and related flow dynamics strongly modify the amount and spatial distribution of precipitation. Various idealised three-dimensional simulations with the non-hydrostatic weather prediction model COSMO using uniform wind and stability profiles have been performed to investigate the relationship between ambient conditions, flow characteristics, and orographic precipitation patterns. A series of simulations with changing wind speed, static stability, temperature, and relative humidity was conducted to reveal how inclusion of moisture affect flow dynamics and how precipitation patterns change with ambient conditions. The parameter range was selected to be representative of mid-latitude stratiform precipitation events over low mountains and capture a wide range from strong upstream deceleration to conditionally unstable flow.

Kunz, Wassermann: Sensitivity of flow dynamics and orographic precipitation to changing ambient conditions in idealised model simulations
Meteorologische Zeitschrift 2 (2011), S. 199-215. 

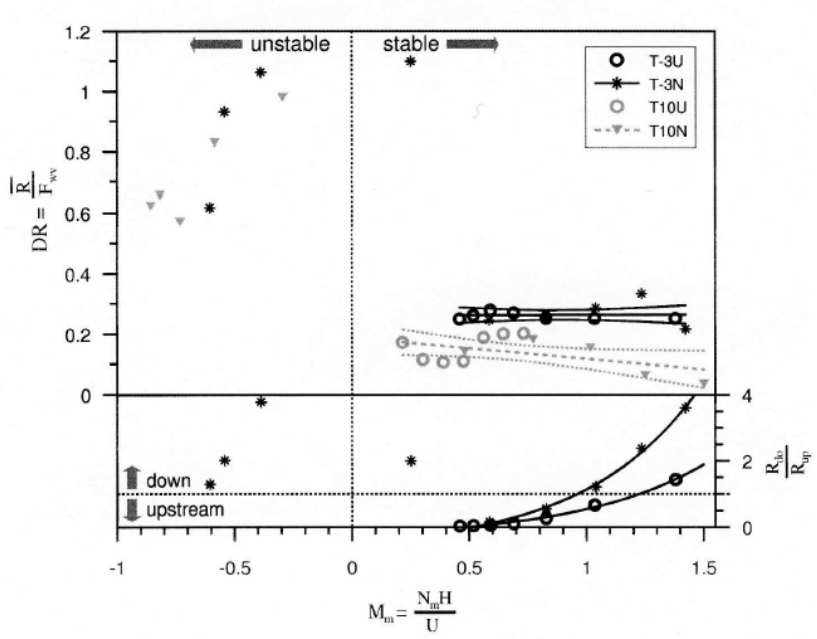


Figure 14: Regime diagram for orographic precipitation: drying ratio *DR* (top of the diagram) from COSMO T-3N, T-3U, T10N, and T10U experiments with regression line and confidence intervals (90% level of significance) and ratio of downstream to upstream precipitation (bottom of the diagram) from T-3N und T-3U experiments as a function of the nondimensional mountain height $M_m$.

The simulations revealed that inclusion of moisture lowers static stability in regions with ascent due to the release of latent heat of condensation. Hence, the onset of upstream flow stagnation is significantly delayed in saturated flows. This delay can be qualitatively understood by considering the moist stability concept (DURRAN and KLEMP, 1982; JIANG, 2003), where the dry Brunt-Väisälä frequency $N_d$ is substituted by the saturated equivalent $N_m$ to quantify the moist nondimensional mountain height $M_m = N_m H/U$ or its inverse, the moist Froude number $Fr_m$. This approach is reasonable for flow deceleration upstream of the mountain, which occurs in a saturated environment due to stable ascent in the lowest layers. Flow blocking, however, indicated by very small or zero *u'*, does not occur within the parameter range considered in this study. This implies that blocking is not relevant during frontal precipitation events over low-mountain ranges. It is shown that the vertical wavelength of the orographically induced gravity waves changes only marginally when the flow becomes saturated. By comparing simulated with calculated wavelengths, it turned out that

the dry solution is much closer to the results than the saturated. This finding does not contradict the applicability of the moist stability concept for flow deceleration prediction since gravity wave response is controlled by a much deeper atmospheric layer, which is characterised by oscillating vertical motions. Resulting alternating shallow saturated and unsaturated layers cannot be fully described by the means of dry as well as moist stability concept.

It is shown that the orographic precipitation distributions depend on the interaction between terrain-induced vertical velocities related to gravity waves and cloud microphysics aloft. During very stably stratified conditions, the precipitation patterns are primarily determined by the extended gravity wave downstream. As the gravity wave tilts up vertically and direct mountain overflow increases for decreasing $M_m$, the precipitation maxima shift from a downstream to an upstream location. Furthermore, the amount and spatial distribution of orographic precipitation is strongly controlled by the ratio between the time scales for mountain overflow $\tau_m$ and that of cloud microphysics and hydrometeor advection $\tau_c+\tau_f$. When $\tau_m > \tau_c+\tau_f$, i.e. when mountain overflow lasts long enough for conversion and fallout processes, most of the precipitation reaches the ground upstream of the crest and precipitation totals are comparable high. This is the case when a mixed-phase cloud with short cloud conversion times $\tau_c$ forms upstream of the mountain or when the flow speed $U$ is low. If $\tau_m < \tau_c+\tau_f$, realised either by a warm cloud with high conversion times or by high wind speed $U$, condensate and hydrometeors are advected downstream of the mountain, where they partly evaporate in descent regions without precipitation reaching the ground.

Both the drying ratio ($DR$), expressing the conversion of the upstream moisture flux into precipitation, and the location of the precipitation maxima are controlled by static stability and flow speed. With increasing wind speed, upstream precipitation increases almost linearly, whereas the secondary maximum downstream weakens. At high wind speeds, higher penetration of the mountain wave together with the flow directed over the mountain leads to an intensification of upstream precipitation. Decreasing static stability, on the other hand, causes an increase in the precipitation totals, but also a change in the location of the maxima. When static stability decrease and the flow regime changes from the flow around to flow over the mountain, the precipitation maxima shift to a location upstream, yielding also higher totals. The transition from stably ascent to shallow convection occurs quite abruptly when $N_m$ becomes imaginary, indicating conditionally moist unstable flow. Marginally unstable air masses impinging on a mountain lead to the development of a stratiform orographic cloud with embedded convection, which substantially increase precipitation intensity on the local scale, as it was also demonstrated by KIRSHBAUM and DURRAN (2004) or FUHRER and SCHÄR (2005).

As long as the atmosphere is stably stratified, orographic precipitation is primarily controlled by the ratio $U/N$ and the incoming moisture flux $F_{wv}$. In that sense, the enhancement of precipitation over mountains can be described to a certain degree by a combination of the two parameters, as it was found over several low mountain ranges in Germany. From the model simulations, it turned out that the drying ratio $DR$ is almost insensitive to variations in the nondimensional mountain height $M_m$, but depend on the ambient temperature and, thus, the moisture load. This means that the results

Kunz, Wassermann: Sensitivity of flow dynamics and orographic precipitation to changing ambient conditions in idealised model simulations S. 214
Meteorologische Zeitschrift 2 (2011), S. 199-215.

are approximately similar irrespective of whether $N_d$ or $U$ was varied. The location of the maxima can also be properly described by $M_m$, but yields two different solutions depending on whether $N_d$ or $U$ were changed. The different solutions indicate that moist flow dynamics, which are decisive for the precipitation regime under the assumption of constant cloud microphysics, can be described satisfactorily neither by dry stability $N_d$ nor by saturated stability $N_m$.

The conclusions drawn in this paper, however, are restricted to the parameter range considered, which is representative for orographic precipitation over midlatitude low-mountain ranges. As shown for example by WASTL and ZÄNGL (2008) or PANZIERA and GERMANN (2010), the findings are not valid for higher mountains like the Alps, where highly non-linear effects may dominate the precipitation distribution. Furthermore, this study did not consider any aerosol impact on condensation processes, which may significantly modify gravity waves and, hence, the amount and spatial distribution of precipitation by release of latent heat according to the COSMO studies performed by MÜHLBAUER and LOHMANN (2008).

## Acknowledgments

This research was supported by a grant of the Deutsche Forschungsgemeinschaft (Ku-1923) within the framework of the priority programme SPP 1167 "Quantitative precipitation forecast". We thank Andreas HENSE and Armin MATHES (University of Bonn) for the organization of the priority programme and Axel SEIFERT and Jochen FÖRSTNER from DWD for helpful discussions and various supports. The authors are grateful to the constructive comments and suggestions of two anonymous reviewers that helped to improve the quality of this paper.

## References

BAINES, P.G., R.B. SMITH, 1993: Upstream stagnation points in stratified flow past obstacles. – Dynam. Atmos. Oceans 18, 105–113.

BARTHLOTT, C., R. BURTON, D. KIRSHBAUM, K. HANLEY, E. RICHARD, J.-P. CHABOUREAU, J. TRENTMANN, B. KERN, H.-S. BAUER, T. SCHWITALL, C. KEIL, Y. SEITY, A. GADIAN, A. BLYTH, S. MOBBS, C. FLAMANT, J. HANDWERKER, in print: Initiation of deep convection at

marginal instability in an ensemble of mesoscale models: A case study from COPS. – Quart. J. Roy. Meteor. Soc.

BAUER, M.H., G.J. MAYR, I. VERGEINER, H. PICHLER, 2000: Strongly nonlinear flow over and around a threedimensional mountain as a function of the horizontal aspect ratio. – J. Atmos. Sci. 57, 3971–3991.

BOLTON, D., 1980: The computation of equivalent potential temperature. – Mon. Wea. Rev. 108, 1046–1053.

CARBONE, R.E., J.D. TUTTLE, W.A. COOPER, V. GRUBISIC, W.C. LEE, 1998: Trade wind rainfall near the windward coast of Hawaii. – Mon. Wea. Rev. 126, 2847–2863.

COLLE, B.A., 2004: Sensitivity of orographic precipitation to changing ambient conditions and terrain geometries: An idealized modeling perspective. – J. Atmos. Sci. 61, 588– 606.

DOMS, G., J. FÖRSTNER, E. HEISE, H.-J. HERZOG, M. RASCHENDORFER, R. SCHRODIN, T. REINHARDT, G. VOGEL, 2007: A description of the nonhydrostatic regional model LM. Part II: Physical parameterization. – Technical report, Consortium for Small-Scale Modelling 139 pp.

DURRAN, D. R., 1990: Mountain waves and downslope winds. – In: W. BLUMEN (Ed.), Atmospheric processes over complex terrain, number 45 in Meteorological Monographs, American Meteorol. Soc., Boston, 59–81.

DURRAN, D.R., J.B. KLEMP, 1982: On the effects of moisture on the Brunt-Väisälä frequency. – J. Atmos. Sci. 39, 2152–2158.

DURRAN, D.R., J.B. KLEMP, 1983: A compressible model for the simulation of moist mountain waves. – Mon. Wea. Rev. 111, 2341–2361.

FRASER, A.B., R.C. EASTER, P.V. HOBBS, 1973: A theoretical study of the flow of air and fallout of solid precipitation over mountainous terrain. Part I: Airflow model. – J. Atmos. Sci. 30, 801–812.

FUHRER, O., C. SCH¨A R, 2005: Embedded cellular convection in moist flow past topography. – J. Atmos. Sci. 62, 2810–2828.

HOUZE, R.A., C.N. JAMES, S. MEDINA, 2001: Radar observation of precipitation and airflow on the Mediterranean side of the Alps: Autumn 1998 and 1999. – Quart. J. Roy. Meteor. Soc. 127, 2537–2558.

JIANG, Q., 2003: Moist dynamics and orographic precipitation. – Tellus 55A, 301–316.

JIANG, Q., R.B. SMITH, 2003: Cloud timescales and orographic precipitation. – J. Atmos. Sci. 60, 1543–1559. KIRSHBAUM, D.J., D.R. DURRAN, 2004: Factors governing cellular convection in orographic precipitation. – J. Atmos. Sci. 61, 682–698.

KIRSHBAUM, D.J., R.B. SMITH, 2008: Temperature and moist-stability effects on midlatitude orographic precipitation. – Quart. J. Roy. Meteor. Soc. 134, 1183–1199.

KUNZ, M., 2011: Characteristics of large-scale orographic precipitation in a linear perspective. – J. Hydrometeorol. 12, 27–44.

KUNZ, M., C. KOTTMEIER, 2006a: Orographic enhancement of precipitation over low mountain ranges. Part I: Model formulation and idealized simulations. – J. Appl. Meteor. Climatol. 45, 1025–1040.

KUNZ, M., C. KOTTMEIER, 2006b: Orographic enhancement of precipitation over low mountain ranges. Part II: Simulation of heavy precipitation events over Southwest Germany. – J. Appl. Meteor. Climatol. 45, 1041–1055.

LALAS, D.P., F. EINAUDI, 1974: On the correct use of the wet adiabatic lapse rate in the stability criteria of a saturated atmosphere. – J. Appl. Meteor. 13, 318–324.

LYRA, G., 1943: Theorie der stationären Leewellenströmung in freier Atmosphäre. – Z. Angew. Math. Mech. 23, 1–28.

MEDINA, S., R.A. HOUZE, 2003: Air motions and precipitation growth in Alpine storms. – Quart. J. Roy. Meteor. Soc. 129, 345–371.

MELLOR, G.L., T. YAMADA, 1982: Development of a turbulence closure model for geophysical fluid problems. – Rev. Geophys. 20, 851–875.

MILES, J. W., H. E. HUPPERT, 1969: Lee waves in stratified flow. Part IV: Perturbation approximations. – J. Fluid Mech. 35, 497–525.

MÜHLBAUER, A., U. LOHMANN, 2008: Sensitivity studies of the role of aerosols in warm-phase orographic precipitation in different dynamical flow regimes. – J. Atmos. Sci. 65, 2522–2542.

PANZIERA, L., U. GERMANN, 2010: The relation between airflow and orographic precipitation on the southern side of the Alps as revealed by weather radar. – Quart. J. Roy. Meteor. Soc. 136, 222–238.

PIERREHUMBERT, R.T., B. WYMAN, 1985: Upstream effects of mesoscale mountains. – J. Atmos. Sci. 42, 977– 1003.

QUENEY, P., 1948: The problem of airflow over mountains: A summary of theoretical studies. – Bull. Amer. Meteor. Soc. 29, 16–26.

SCHÄR, C., D.R. DURRAN, 1997: Vortex formation and vortex shedding in continuously stratified flows past isolated topography. – J. Atmos. Sci. 54, 534–554.

SCHÄTTLER, U., A. S. C. DOMS, G., 2007: A description of the nonhydrostatic regional COSMO-Model, Part VII: User's Guide. – Technical report, available at www.cosmomodel. org.

SEIFERT, A., K.D. BEHENG, 2006: A two-moment cloud microphysics parameterization for mixed-phase clouds. Part 1: Model description. – Meteor. Atmos. Phys. 92, 45–66.

SHEPPARD, P.A., 1956: Airflow over mountains. – Quart. J. Roy. Meteor. Soc. 82, 528–529.

SINCLAIR, M. R., D. WRATT, R. HENDERSON, W. GRAY, 1997: Factors affecting the distribution and spillover of precipitation in the southern Alps of New Zealand – A case study. – J. Appl. Meteor. 36, 428–442.

SMITH, R.B., 1979: The influence of mountains on the atmosphere. – Adv. Geophys. 21, 87–230. —, 1980: Linear theory of stratified hydrostatic flow past an isolated mountain. – Tellus 32, 348–364. —, 1989: Hydrostatic airflow over mountains. – Adv. Geophys. 31, 1–41.

SMITH, R.B., I. BARSTAD, 2004: A linear theory of orographic precipitation. – J. Atmos. Sci. 61, 1377–1391. SMITH, R.B., S. GRØNÅS, 1993: Stagnation points and bifurcation in 3-D mountain airflow. – Tellus 45A, 28–43.

SMITH, R.B., I. BARSTAD, L. BONNEAU, 2005: Orographic precipitation and Oregons climate transition. – J. Atmos. Sci. 62, 177–191.

SMOLARKIEWICZ, P. K., R. ROTUNNO, 1989: Low Froude number flow past three-dimensional obstacles. Part I: Baroclinically generated lee vortices. – J. Atmos. Sci. 46, 1154– 1164.

STEINER, M., O. BOUSQUET, R. A. HOUZE, B. F. SMULL, M. MANCINI, 2003: Airflow within major Alpine river valleys under heavy rainfall. – Quart. J. Roy. Meteor. Soc. 129, 411–431.

STELLER, H., 2004: Analyse und Simulation des orografisch bedingten Niederschlags ¨uber Mittelgebirgen. – Master's thesis, University of Karlsruhe.

ULBRICH, U., T. BRÜCHER, A. H. FINK, G. C. LECKEBUSCH, A. KRÜGER, J. G. PINTO, 2003: The central European floods of August 2002: Part I – Rainfall periods and flood development. – Weather 58, 371–377.

WASTL, C., G. Z¨A NGL, 2008: Analysis of mountain-valley precipitation differences in the Alps. – Meteorol. Z. 17, 311–321.

WEISMAN, M., W. SKAMAROCK, J. KLEMP, 1997: The resolution dependence of explicitly modeled convective systems. – Mon. Wea. Rev. 125, 527–548.

WICKER, L.J., W.C. SKAMAROCK, 2002: Time-splitting methods for elastic models using forward time schemes. – Mon. Wea. Rev. 130, 2088–2097.

WURTELE, M., 1957: The three-dimensional lee wave. – Beitr. Phys. Atmos. 29, 242–252.

ZÄNGL, G., 2008: The temperature dependence of smallscale orographic precipitation enhancement. – Quart. J. Roy. Meteor. Soc. 134, 1167–1181.